NeuroImage 191 (2019) 560–567

Contents lists available at ScienceDirect

NeuroImage

journal homepage: www.elsevier.com/locate/neuroimage

PET imaging of freely moving interacting rats

Alan Miranda [a], Min Su Kang [b,d], Stephan Blinder [d], Reda Bouhachi [d], Jean-Paul Soucy [d], Arturo Aliaga-Aliaga [b,d], Gassan Massarweh [d], Sigrid Stroobants [a,c], Steven Staelens [a], Pedro Rosa-Neto [b,d], Jeroen Verhaeghe [a,*]

[a] Molecular Imaging Center Antwerp, University of Antwerp, Universiteitsplein 1, 2610, Antwerp, Belgium
[b] Translational Neuroimaging Laboratory, McGill University Research Centre for Studies in Aging, Douglas Mental Health University Institute, 6875 Boulevard LaSalle, Montreal, QC, H4H 1R3, Canada
[c] University Hospital Antwerp, Wilrijkstraat 10, 2650, Antwerp, Belgium
[d] Montreal Neurological Institute, McGill University, 3801 University Street, Montreal, QC, H3A2B4, Canada

ARTICLE INFO

Keywords:
Motion correction
Molecular imaging
Neurology

ABSTRACT

Awake rat brain positron emission tomography (PET) has previously been developed to avoid the influence of anesthesia on the rat brain response. In the present work, we further the awake rat brain scanning methodology to establish simultaneous scanning of two interacting rats in a high resolution, large field of view PET scanner. Awake rat imaging methodology based on point source tracking was adapted to be used in a dedicated human brain scanner, the ECAT high resolution research tomograph (HRRT). Rats could freely run on a horizontal platform of 19.4 × 23 cm placed inside the HRRT. The developed methodology was validated using a motion resolution phantom experiment, 3 awake single rat [^{18}F]FDG scans as well as an [^{18}F]FDG scan of 2 interacting rats. The precision of the point source based motion tracking was 0.359 mm (standard deviation). Minor loss of spatial resolution was observed in the motion corrected reconstructions (MC) of the resolution phantom compared to the motion-free reconstructions (MF). The full-width-at-half-maximum of the phantom rods were increased by on average 0.37 mm in the MC compared to the MF. During the awake scans, extensive motion was observed with rats moving throughout the platform area. The average rat head motion speed was 1.69 cm/s. Brain regions such as hippocampus, cortex and cerebellum could be recovered in the motion corrected reconstructions. Relative regional brain uptake of MC and MF was strongly correlated (Pearson's r ranging from 0.82 to 0.95, $p < 0.0001$). Awake rat brain PET imaging of interacting rats was successfully implemented on the HRRT scanner. The present method allows a large range of motion throughout a large field of view as well as to image two rats simultaneously opening the way to novel rat brain PET study designs.

1. Introduction

Positron emission tomography (PET) is used to image physiological and biochemical processes (e.g. glucose metabolism) *in vivo* in humans and in animal models in preclinical research. This imaging technique is the gold standard method for quantifying neurochemistry and molecular processes directly in the brain by injecting a radiopharmaceutical that specifically targets the processes of interest. However, the use of anesthesia to keep animals in the same position within the field of view of the tomograph constitutes an important limitation which has a direct impact on PET outcomes. Overcoming these limitations could advance the animal imaging field toward the simultaneous investigation of social dynamics and models of psychiatric conditions at the neurochemical level. Thus, in order to circumvent these limitations, Schulz et al. (2011) advanced the small PET imaging field by successfully and simultaneously assessing neurochemistry and the general behavior of small animals while awake using a helmet called RatCAP. However, RatCAP requires a surgical procedure to ensure its stability in addition to a mechanical arm which relieves pressure on the rat's head. Two other methods involve head restraining (Mizuma et al., 2010) and the use of motion-tracking devices (Kyme et al., 2008; Spangler-Bickell et al., 2016) to perform scans of awake animals, both of which necessitate some degree of restriction or significant habituation protocols that could interfere with the quantification of certain biological phenomena. To date, no method has allowed for the simultaneous assessment of multiple freely and naturally interacting animals.

* Corresponding author.,.
E-mail address: jeroen.verhaeghe@uantwerpen.be (J. Verhaeghe).

https://doi.org/10.1016/j.neuroimage.2019.02.064
Received 11 December 2018; Received in revised form 6 February 2019; Accepted 25 February 2019
Available online 2 March 2019

Here, we propose a method for performing PET scans of free-running rats inside a large acrylic glass imaging cage without the need for any surgical intervention and using a high-resolution human brain PET scanner, i.e., the high-resolution research tomograph (HRRT, CTI/Siemens). Our method tracks the motion of the rat's head during the PET scan by using four small, lightweight positron-emitting point sources attached to the rat's head as markers (Miranda et al., 2017). In contrast with free running rat PET scans using optical tracking methods (Kyme et al., 2018), the current method does not require to perform a spatial and temporal calibration between the tracking system and the PET scanner. In addition, the tracking system does not suffer from camera occlusion from the scanner bore, allowing to track the rat throughout the scanner's field of view (FOV), irrespective of the rat's head pose. Importantly, the use of a large FOV scanner allows to perform scans of interacting rats. The point source tracking method also facilitates tracking of interacting rats, which might be challenging using optical tracking methods due to camera occlusion by the body of the other rat. The motion-corrected images are reconstructed from the PET tracking measurements after image acquisition.

In order to ensure that the motion-corrected reconstructions have the same spatial resolution as motion-free reconstructions, we first performed a resolution phantom experiment to assess the spatial resolution of motion-corrected reconstructions. We then performed three scans of single free-running rats and a scan of two interacting rats simultaneously inside the scanner's FOV. The glucose analog [^{18}F]FDG was used for validation purposes since the brain uptake remains approximately constant after an uptake period of about 30 min, allowing comparison of an awake scan with a subsequent motion-free (under anesthesia) scan. The ability to conduct PET scans of freely and naturally running animals with accurate quantification could open up new research avenues and introduce a novel experimental paradigm across various disciplines.

2. Methods

2.1. Scanner

All of the experiments were performed on a high-resolution research tomograph (HRRT, CTI/Siemens) (de Jong et al., 2007). The scanner's FOV was 312 mm in diameter with an axial length of 250 mm. The spatial resolution of the HRRT varies from 2.3 mm in the center of the FOV (CFOV) to 3.2 mm toward the edge. The absolute sensitivity is 2.9% at the CFOV.

2.2. Motion tracking

The positron-emitting point sources used for the motion tracking were made from sodium polyacrylate grains. Grains measuring less than 1 mm in diameter were manually selected to create the point sources. First, the grains were soaked in hematoxylin colorant for 10 s for better visualization before being soaked in [^{18}F]FDG for 5 s. Each point source's activity was measured in a dose calibrator and if the desired activity level had not been reached, it was soaked again in [^{18}F]FDG. This procedure was repeated until the desired activity was reached. Only point sources with an activity level of between 259 and 333 kBq were considered as position markers.

The motion-tracking algorithm used was an extension of the method previously developed by our group for the Siemens Inveon scanner (Miranda et al., 2017). Modifications to the original method were required to handle the larger FOV, lower sensitivity and lower spatial resolution of the HRRT compared to the Inveon scanner. In summary, in comparison with the implementation in the Inveon scanner, the point source activity was increased due to the lower scanner sensitivity and the method to detect the point sources in short time frames was changed from a shape similarity metric, which does not perform well in lower resolution images, to a consistent motion metric. The tracking algorithm is detailed below.

The motion-tracking algorithm was run after the acquisition was completed. The list-mode data of the motion scan was divided into short (32 ms) time frames. Each time frame, i, was then processed consecutively. First, the frame was reconstructed using MLEM list-mode reconstruction (Rahmim et al., 2004b), without attenuation or scatter correction, consisting of four iterations and filtered with a Gaussian filter with a kernel size of 5 voxels and a standard deviation of 1.1 voxels. The obtained image, measuring 256 × 256 × 207 voxels (voxel size 1.22 mm), was denoted as f^i ($i = 1 \ldots I$).

Before we could begin tracking, we had to define a model of the point sources. The position of each point source was semi-automatically located in one of the time frames, and their inter-point distances were recorded as a model. The number of point sources p ($p = 1 \ldots P$, typically $P = 4$) and their inter-point distances m_l ($l = 1 \ldots L$), were recorded to initialize the tracking algorithm. In addition, the intensity at the point source locations a_p was recorded, and the distance b_p from every point to the plane that best fitted (least square fitting) the group of points was calculated for later use in the tracking algorithm.

The actual tracking then began with the first frame (f^1). Next, because the point sources are local maxima which have a high intensity in the reconstructed image, all of the local maxima were located in the image by first performing a gray-scale dilation:

$$f^{i,d} = f^i \oplus \kappa \tag{1}$$

where κ is a 5 × 5 × 5-voxel kernel with a value of 1 for all voxels except the central voxel, which had a value of 0. The local maxima were then identified by selecting voxels for which $f^i > f^{i,d}$. Since the intensity of the local maxima corresponding to the point sources was higher than that of most local maxima present in the image, only the points with the 60 highest intensities were retained. Using the remaining local maxima, the number of points was reduced further by the fact that the local maxima corresponding to the point sources in consecutive frames would be located nearby. On the other hand, most of the other local maxima tended to be randomly redistributed between two consecutive frames due to image noise. Therefore, from frame 3, the distances from all local maxima in the frame $i - 2$ to all local maxima in the frame $i - 1$ were calculated. Only the local maxima in frame $i - 1$ whose distances to the closest local maxima in frame $i - 2$ was below a predefined threshold (8 mm in our experiments) were retained. The distances from the remaining local maxima in frame $i - 1$ to all the local maxima in frame i were then calculated. Again, only those local maxima in frame i whose distances to the closest points in frame $i - 1$ were below the threshold (<8 mm) were retained. Finally, a score was calculated for all of the remaining local maxima in frame i as the sum of the distance to the closest point in frame $i - 1$ and the distance from that point to its closest point in frame $i - 2$. Only the 20 points with the lowest scores were retained for further processing by the algorithm. For the first two frames (for which not enough previous frames were available), the number of points was not reduced, i.e., 60 points were used in the next step.

Using the remaining 20 local maxima (60 for frames 1 and 2), we considered each combination (group) n ($n = 1 \ldots N$) of P points whose inter-point distances D_l^n were below the threshold difference (3 mm in our experiments) from the model m_l inter-point distances. A score was calculated for each group n as

$$S_n = w_1 \sum_l \left| D_l^n - m_l \right| + w_2 \sum_p \left| E_p^n - a_p \right| + w_3 \sum_p \left| F_p^n - b_p \right| \tag{2}$$

where E_p^n is the intensity of the p -th point in group n, F_p^n is the distance from point p to the plane that best fits the group n, and w_1, w_2 and w_3 are weights empirically set to $5e^{-2}$, $3e^{-3}$ and 0.2, respectively, for all the experiments. The group of points n that minimizes S_n were selected as the correct point sources. If no group's inter-point distances were below the preset threshold (3 mm) or score S_n was not below a maximum value (4 in our experiments), we considered the tracking to have failed in that frame.

The tracking success rate, i.e. the percentage of frames that were successfully tracked, is reported.

The position of each correctly tracked point source, initially defined as the center of the voxel of the local maximum, was then refined further. The final position was defined as the point that minimizes the distance to LORs associated with the point source (Parker et al., 1993). These LORs were selected as the LORs that pass within 3 mm of the voxel center.

To reduce the processing time, if the point sources had been identified correctly in the preceding frame, the current frame was reconstructed in the bounding box that enclosed the point sources in the previous frame plus an additional margin of 10 voxels in all three directions. Therefore, the image size of the short frames varied according to the point sources' positions. In addition, if the preceding frame had been correctly tracked and if a local maximum in the current frame was close (<3 mm in our experiments) to one of the point source locations in the preceding frame, this local maximum was selected as one of the correct point source locations in the current frame.

Once the point sources had been tracked in the short time frames, the pose in each frame was calculated. The pose encompass the six degrees of freedom describing the position (x, y, z) and orientation/rotation (Euler angles α, β, γ) of the object on which the point sources are attached. The position of the pose was defined as the centroid of the point sources and the orientation was determined by calculating the transformation to the model point sources using singular value decomposition of the points sources coordinates cross-covariance matrix (Besl and Mckay, 1992).

If the inter-point distances had changed slightly, e.g., due to the rat's skin slipping over its skull, or if the point sources' intensity had decreased due to radioactive decay, the model values m_l, a_p and b_p would differ from the actual values. To correct these effects, the model inter-point distances m_l, intensities a_p and point-plane distances b_p were constantly recalculated as the mean of the values in the previous five correctly tracked frames. Furthermore, to avoid the use of erroneously calculated poses due to point source slippage (change in point source geometry), the reliability of a pose was determined as follows. If after registration to the model, the distance from any point source in a given frame to the corresponding model point source was more than 3 mm, the pose in that frame was considered erroneous and not included in the motion correction reconstruction.

When tracking two subjects simultaneously, the geometry of their groups of point sources must be different enough to be able to differentiate between them. We found that a difference in the inter-point distances between the two point source groups of at least 2–3 times the scanner's spatial resolution was sufficient to differentiate between the two subjects in our experiments. Satisfying this condition, the two groups of point sources can be tracked independently with the same algorithm used for tracking a single subject. Fig. 1 summarizes the motion tracking algorithm.

2.3. Walking path calculation

The trajectory of the rat motion was calculated from the short time frame reconstructions. We first calculated the projection in the x - z (horizontal) plane for each time frame. Next, each frame projection was processed sequentially. An optimal threshold (Otsu, 1979) was calculated in order to obtain a binary image in which the rat body activity was segmented from the background. To eliminate outliers, Euclidian clustering (Rusu and Cousins, 2011) was carried out and the cluster with the largest size was selected as belonging to the rat body. Binary morphological transformations (Gonzalez and Woods, 2002) were then performed to fill the holes in the rat body cluster, to obtain the body outline and to smoothen it. The rat position was calculated as the geometric centroid of the body outline. Finally, the rat body positions were filtered in time with a symmetric Gaussian filter (σ = 80 ms) and the walking path was calculated using the difference in position between the frames.

2.4. Image reconstruction and quantification

The total data set was reconstructed into a single static frame using our in-house developed software. Motion-free scans were reconstructed with ordered subset list-mode (LM-EM) reconstruction (Rahmim et al., 2004b), while motion-corrected images were reconstructed using LM-EM motion-compensated reconstruction (Rahmim et al., 2004a). Both of these methods considered 16 subsets and 8 iterations, including image-space-based resolution modeling (Reader et al., 2003) using a Gaussian with a full-width-at-half-maximum (FWHM) of 3 mm. The motion-compensated sensitivity image was calculated through trilinear interpolation in the image space as described in Rahmim et al. (2004a). No scatter correction was performed since it affects minimally to rat brain regional quantification (Spangler-Bickell et al., 2016).

Attenuation correction in the motion-free and motion-corrected reconstructions was performed by calculating the attenuation map based on the image segmentation of the rat body activity volume (Angelis et al., 2013), assuming a constant attenuation factor for soft tissue (0.096 cm^{-1}) for the entire body. In the motion-corrected images, the body outline was incorrectly defined due to the independent motion of the body from the head. The independent body motion was translated into a blurry activity image of the body, which occupied more volume than the rat's true body volume. In order to obtain the correct body

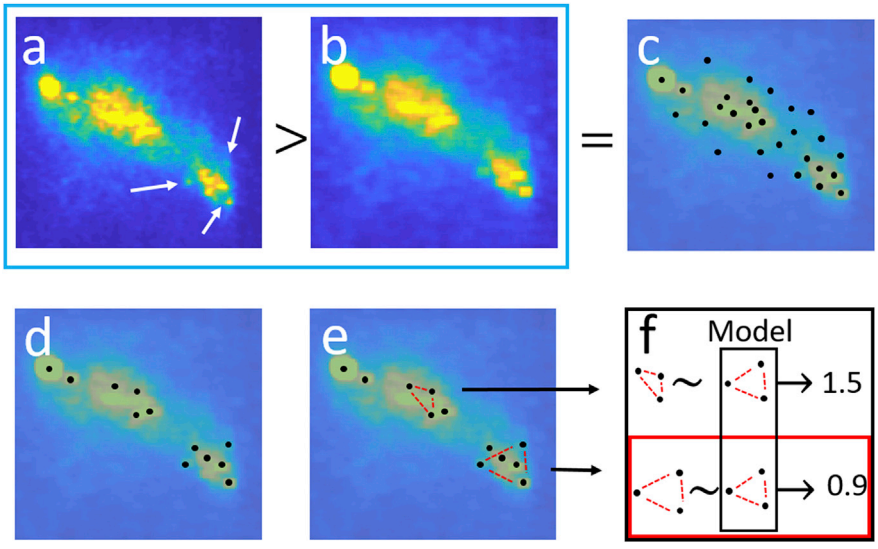

Fig. 1. A diagram of the motion-tracking algorithm performed for every frame. (a) Initially, the 32 ms time frame is reconstructed. The white arrows indicate the point sources to be detected. (b) Next, the gray-scale dilation of the frame is calculated. (c) Pixels in the original image whose intensity is greater than the dilated image represent the local maxima, i.e., the probable point sources. (d) The number of local maxima is reduced further based on an intensity threshold and by comparing the position of the local maxima with the local maxima in the previous frame. Only the local maxima located close (<8 mm) to the local maxima in the previous frame are retained. (e) The remaining local maxima are used to create clusters of points with the same number of points as the model. (f) The cluster of points that minimizes an error metric is selected as the correct cluster of point sources in that frame.

volume from the motion-corrected segmented image, a region-growing algorithm was used to gradually increase the volume of the attenuation image until the attenuation map volume matched the rat's volume. This was achieved by first considering the complete segmented binary image of the rat's body activity and then performing Euclidian clustering with an initialization seed in the rat's brain, growing the image volume gradually until the volume of the rat's body matched. The rat's volume was calculated from the animal's weight, measured prior to the experiment, and assuming a constant soft tissue density for the whole body.

2.5. Resolution phantom experiment

A resolution phantom experiment was carried out to evaluate the spatial resolution of the motion-corrected reconstructions. A hot-rod phantom (Data Spectrum Corporation, Micro Hot Spot ECT Phantom) with rod diameters of 1.2, 1.6, 2.4, 3.2, 4.0 and 4.8 mm was filled with 37 MBq of [^{18}F]FDG. Three point sources were pasted onto the phantom Plexiglas case to track its motion. The inter-point distances were 34.4, 76.5, and 66.6 mm. The phantom was placed on a horizontal platform inside the scanner bore and manually moved through the scanner's FOV in the x - z plane (horizontal plane) for 20 min. The phantom was moved with an average speed of 4.31 cm/s. Subsequently, a 20-min motion-free scan was performed for comparison.

The position of the resolution phantom was represented in a 2D (x - z) histogram. The origin of the histogram corresponded to the CFOV. A logarithmic scale was used to visualize areas which had short residing times. In addition, the average speed of the phantom was calculated for the entire scan.

Twenty-five transaxial slices through the rods were summed, and the FWHM in the radial direction was calculated for the 2.4, 3.2, 4.0 and 4.8 mm rod sizes by fitting a Gaussian to the rod profile. The FWHM, averaged over rods of the same size, was reported for the motion-corrected and motion-free reconstructions. In addition, the standard deviation (SD) of the motion-tracking position and orientation measurements was calculated from 100 frames of a static phantom position.

2.6. Awake rat brain experiments

2.6.1. HRRT awake rat scanning cage

A Plexiglas imaging cage was designed to restrict the motion of the awake rats to the FOV of the HRRT scanner (Fig. 2). The cage was cylindrical in shape with square lids that fitted firmly to the scanner bore. A plastic grid platform was placed inside the cage, so that the rat was positioned approximately in the horizontal center of the FOV. The area in which the rat could move measured 19.4 cm along the x -axis and 23 cm on the z -axis. The height (along the y -axis) was 15 cm at the center of the cage. Perforations in the grid allowed for urine to drain to the bottom of the cage. Ventilation holes were located at both ends of the cage.

2.6.2. Awake rat brain scans

Three male Long-Evans rats were used for the awake scan experiments. Rats 1, 2 and 3 weighed 350, 360 and 340 g, respectively. All of the procedures described here were performed in accordance with the Canadian Council on Animal Care guidelines and were approved by a McGill Animal Care ethics committee. All of the rats were housed at the Douglas Mental Health University Institute animal facility on 12/12 h light/darkness cycles and *ad libidum* access to food and water. All animals were fasted at least 12 h before the start of the scan. Each rat was first anesthetized with isoflurane in medical oxygen (5% for induction, 2% for maintenance). The rat was then shaved below the ears and on the nasal bridge. Two point sources were affixed to the nasal bridge and two below the ears by placing a drop of cyanoacrylate glue on the shaved areas. [^{18}F]FDG was then administered by tail vein injection. Rats 1, 2 and 3 were administered 19.7, 19.8 and 23.9 MBq respectively. Anesthesia was stopped immediately after the injection and the rat was placed inside the Plexiglas cage for 30 min tracer uptake. Next, the cage was placed inside the HRRT bore and the awake rat was scanned for 20 min. After the awake scan, the rat was anesthetized with R-(−)-Deprenyl hydrochloride using a dose of 0.8 ml per 1000 g to enable us to perform a 20-min motion-free scan for comparison. Fig. 3 shows the time diagram of the animal PET scans.

2.6.3. Simultaneous scan of two awake rats

Two awake Long-Evans rats (Rats 4 and 5) were scanned simultaneously. Rats 4 and 5 weighed 490 and 420 g, respectively. We again followed the scan protocol described above to obtain a 20-min awake scan and a 20-min under anesthesia, motion-free scan for comparison. Rats 4 and 5 were administered 22.6 and 19.6 MBq of [^{18}F]FDG, respectively, by tail vein injection.

2.6.4. Rat brain image analysis

The motion of the rats' heads was analyzed in the same way as the resolution phantom motion (calculation of positions 2D histogram, and average head speed). The motion-corrected reconstructions (MC) and the corresponding reference motion-free reconstructions (MF) were analyzed using PMOD 3.3 (PMOD technologies Ltd, Zurich, Switzerland). The MC was registered to an [^{18}F]FDG brain atlas (Schiffer et al., 2006) through rigid body transformation. The atlas and the corresponding predefined VOIs were then spatially normalized to this image. Finally, the MF was also rigidly transformed to the registered MC image.

The relative [^{18}F]FDG uptake, normalized to the cerebellum, in 60 brain regions defined in the brain atlas (including the hypothalamus, cingulate cortex and hippocampus) was calculated. The Pearson's correlation coefficient between the MF and MC uptake was calculated using all of the brain regions ($n = 60$) and a two-tailed p -value ($p < 0.05$ were considered significant). Statistical analysis was performed using GraphPad Prism 6.0 (GraphPad Software, California, USA).

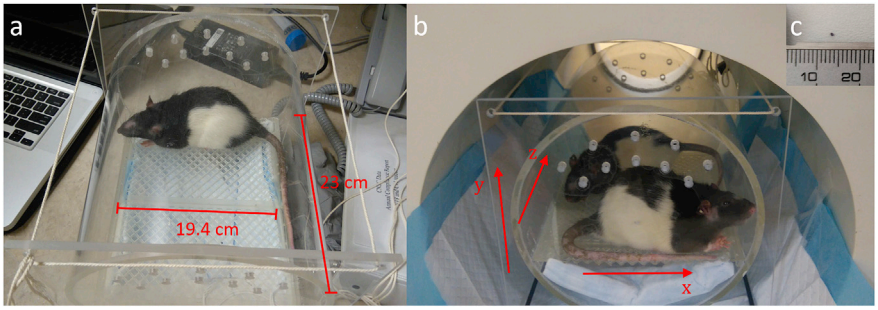

Fig. 2. A dedicated Plexiglas cage was specially designed for the imaging experiments. (a) The cage platform measured 19.4 × 23 cm. The rat could move across a horizontal grid which contained small holes to allow radioactive urine to be evacuated to the bottom of the cage. (b) The cage fitted inside the scanner bore and spanned the FOV. Both ends of the cage contained ventilation holes. (c) One of the point sources used for the motion tracking (scale in mm).

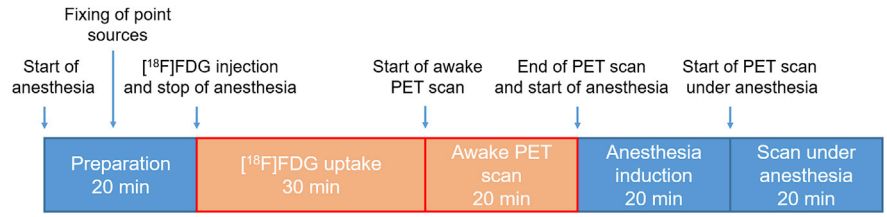

Fig. 3. Time diagram of the rat PET scans protocols. Blue regions indicate periods under anesthesia while orange regions indicate awake periods.

3. Results

3.1. Image resolution of the motion-corrected images

The phantom was moved continuously in random directions at an average speed of 4.31 cm/s (Fig. 4a) across a horizontal platform spanning the scanner's FOV. The tracking success rate was 84%. Fig. 4b shows the histogram of the phantom's positions throughout the entire scan on the horizontal plane. Fig. 5c and d shows the motion-free and motion-corrected reconstructions of the hot-rod phantom, respectively. Fig. 5e shows profiles through the 4 mm rods. The smallest rod size resolved was 2.4 mm. The difference in the rods' full width at half maximum (FWHM) between the motion-free and motion-corrected reconstructions of the phantom had a maximum value of 0.74 mm for the 2.4 mm diameter rods (Fig. 5b), which was three times lower than the scanner's spatial resolution, and a minimum value of 0.06 mm for the 4.8 mm rods.

3.2. Awake rat brain experiments

During the single rat scans, the rats exhibited exploratory behavior typical in a new environment for some periods of time, with recurrent changes in posture and sniffing behavior. Additionally, they remained motionless for long periods of time. The position histograms are shown in Fig. 6a–c. The average speed of each rat's head, measured at a point in the medial prefrontal cortex, was 2.14, 1.36 and 1.46 cm/s for Rats 1, 2 and 3, respectively (Fig. 6d–f). The distance traveled by the rats during the PET scan was measured using the outline of the rat's body activity in the short time frames (Supplemental Video 1). Rats 1, 2 and 3 traveled 21, 15 and 14.9 m during the 20-min scan time, respectively. The tracking success rate was 81%, 54% and 90% for rats 1, 2 and 3 respectively. The low tracking success rate of rat 2 was due to low activity of one of the point sources. The behavior of Rat 1 was considerably more erratic, with long periods of grooming behavior, in comparison to the behavior of Rats 2 and 3, which remained calm during most of the scan with some periods of exploratory behavior (Supplemental Video 2).

In the simultaneous scan of two rats (Rats 4 and 5), both rats remained calm throughout the scan, exploring the cage for brief periods of time. The rats remained with their heads close to the edge of the cage for most of the scan. For some periods of time, their heads overlapped in the x - z plane, when one rat was on top of the other (Supplemental Video 3). The average head speed of the rats was 1.76 and 1.75 cm/s for Rats 4 and 5, respectively. Rats 4 and 5 traveled 12.7 and 13.0 m respectively during the 20-min scan time. The tracking success rate was 84% and 90% for rats 4 and 5 respectively.

3.3. Quantification of awake rat brain experiments

Motion-corrected and motion-free reconstructions of the rats' brains are shown in Fig. 7a. The regional uptake in the rats' brains, normalized to the cerebellum, was calculated for all five rats in both the awake and anesthetized reconstructions. A rat brain atlas (Schiffer et al., 2006) with 60 brain regions, including the hippocampus, cortex and hypothalamus, was used to define and calculate the mean [^{18}F]FDG uptake in different regions. The typical rat brain [^{18}F]FDG uptake shape could be observed in both the motion-free and motion-corrected reconstructions, with a high uptake in certain regions such as the cerebellum, cortex and hippocampus. Considering all of the 60 brain regions, the Pearson's r correlation coefficient between the motion-free and motion-corrected reconstructions of regional brain uptake in Rats 1–5 was 0.86, 0.92, 0.89, 0.89 and 0.82 ($p^{****} < 0.0001$), respectively (Fig. 7b and c). In addition, the time activity curves for the whole brain, caudate putamen and cortex are shown in Fig. 8 for Rat 1, 3 and 4. The TACs show the steady state uptake in the awake scans while under anesthesia TACs show the brain [^{18}F]FDG uptake wash-out (Miranda et al., 2018; Spangler-Bickell et al., 2016).

4. Discussion

We developed a method for performing brain PET imaging in awake, freely running rats for single or multiple naturally interacting rats. Unlike similar awake rat brain PET methods, our approach requires no surgical intervention in the rats and no additional hardware other than the PET scanner itself. By attaching positron-emitting point sources to the rat's head and detecting the points in short time frame reconstructions, the motion of the rat's head can be determined. The motion-tracking data are then used to correct the PET data for motion and obtain reconstructions unaffected by motion artifacts, leading to the generation of accurately quantifiable images.

It was necessary to fabricate the point sources using a radiotracer with an isotope that had a reasonably long half-life, such as [^{18}F]FDG, in order to be able to maintain a high activity in the point sources throughout the scan. Due to the ready availability of [^{18}F]FDG in most PET facilities, the

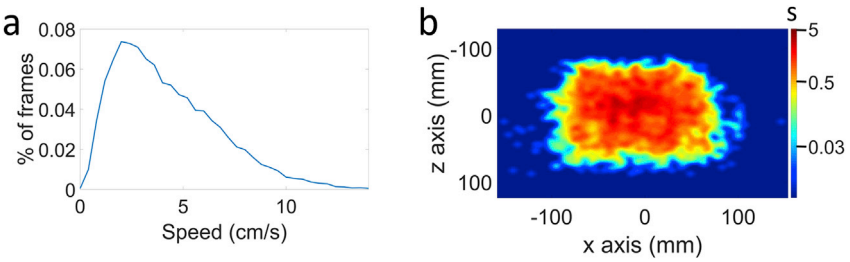

Fig. 4. (a) A histogram of the phantom velocity during the PET scan. (b) A histogram showing the positions of the phantom motion on the horizontal plane (colorscale in seconds).

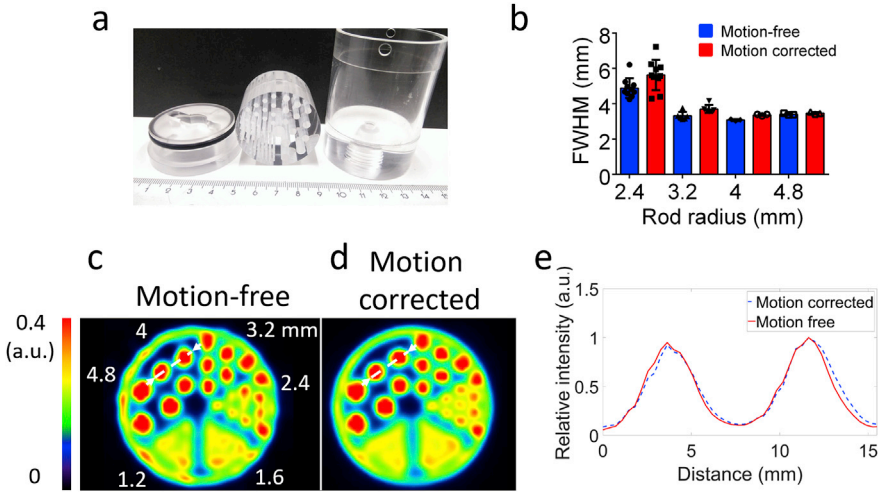

Fig. 5. (a) The hot-rod phantom used to quantify the spatial resolution in motion-corrected reconstructions. The phantom rods' diameters were 1.2, 1.6, 2.4, 3.2, 4 and 4.8 mm. Ruler units in cm. (b) The average FWHM of the phantom rods (mean ± SD) in the motion-free and motion-corrected reconstructions. Transverse slice of the (c) motion-free and (d) motion-corrected scan after the motion correction reconstructions of the hot-rod phantom. (e) Profiles through the dashed white lines indicated in panel (c–d).

creation of the point sources should not represent any difficulties.

Four point sources were used in the animal experiments, whereas only three were used in the phantom scan. The additional point source could serve to increase the accuracy of the motion tracking, as more points are averaged to calculate the rat's head pose. Moreover, if the rat dislodges one of the point sources, the tracking can still be performed with the remaining three point sources. Dislodging occurred in only one of the five rat experiments described here.

The tracking success rate was greater than 80% in most experiments. Only for rat 2, the tracking success rate was low (54%). This was caused by the low activity of one of the point sources which hindered its visualization in the reconstruction of the short time frames. Therefore, special care must be taken to prepare the point sources with enough activity (at least 259 kBq) to avoid tracking failure.

We showed that the motion tracking was accurate enough to avoid excessive loss of spatial resolution in the motion-corrected reconstructions. In a hot-rod resolution phantom experiment, the phantom's rods' FWHM increased by an average of 0.37 mm after motion correction in comparison to the phantom motion-free reconstruction rods. The tracking standard deviation was 0.36 mm, i.e., six times smaller than the scanner spatial resolution (2.3 mm).

The cage was designed to keep the rats inside the scanner's FOV and allowed the rats to move freely and naturally in all directions. During the awake scans, the rats showed no signs of discomfort. Rat 1 did exhibit grooming behavior during most of the awake scan, probably due to the presence of the point sources. Rats 2 and 3 displayed almost no grooming behavior and actively explored the cage on several occasions (Supplemental Video 2). During the scan of two rats, the animals were in close proximity to each other and exhibited some interaction, such as scratching and sniffing behaviors (Supplemental Video 3). Moreover, for a long period of time, one rat rested directly on top of the other. Of these observed behaviors, only excessive grooming could affect the tracking of the point sources, since this behavior stretches the skin of the head and changes the point sources' geometry from a rigid configuration. This behavior could be prevented by habituating the rats to wearing the point sources. Nevertheless, the motion-corrected reconstructions were barely affected by this behavior, as evidenced by the comparison to the motion-free reconstructions.

Although the point sources were placed on the rats under anesthesia in the current experiments, we had previously succeeded in positioning the point sources on awake rats after some training. This removes the need for anesthesia, provided that awake injection of the tracer is performed, for instance, through an implanted catheter (Jespersen et al., 2012).

Quantitative rat brain motion-corrected reconstructions were obtained. An estimated attenuation map was used for attenuation correction. Due to the non-rigid motion of the rat body with respect to the head, the estimated attenuation map is an approximation of the true attenuation map. This might introduce errors in the reconstruction of the brain activity. However, since the posture of the rat head with respect to the body usually changes sporadically and most of the time the head posture remains the same, the approximation of a rigid attenuation map might be sufficient. As it can be seen in the good correlation between motion-free and motion corrected reconstructions regional brain quantification in

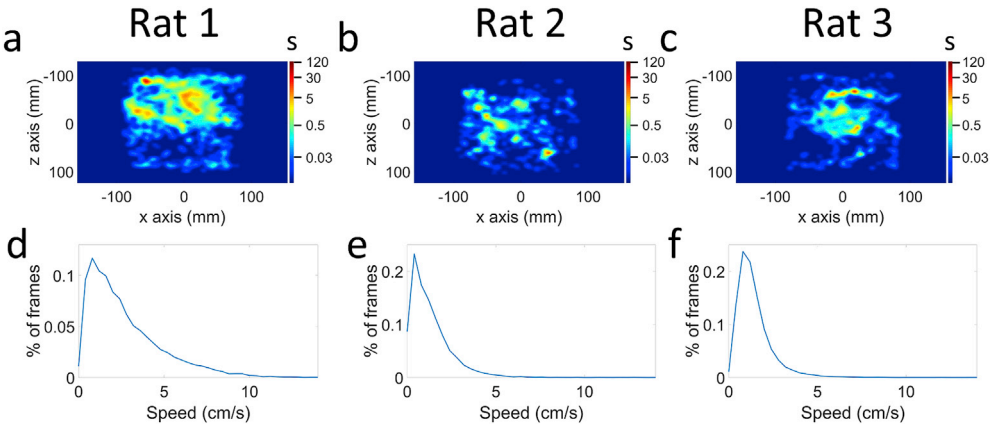

Fig. 6. The position histogram on the *x* - *z* plane (horizontal plane) during the PET scan for (a) Rat 1, (b) 2 and (c) 3. The speed histogram for the motion during the PET scan for (d) Rat 1, (e) 2 and (f) 3. Position and speed were calculated for a point inside the medial prefrontal cortex.

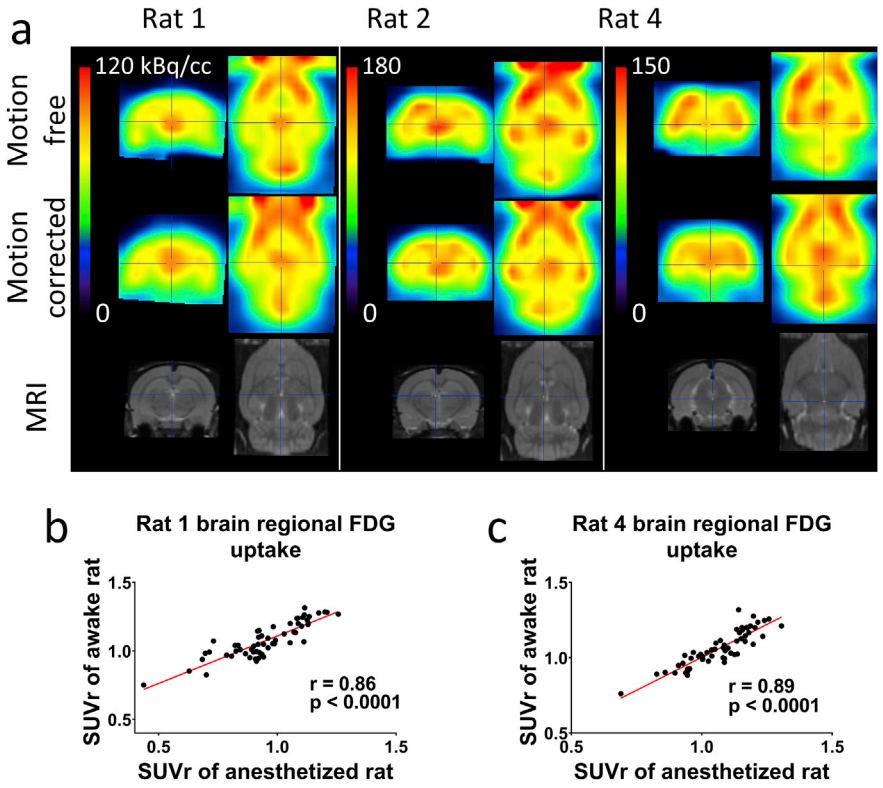

Fig. 7. (a) Coronal and transverse slices of the rat brain reconstructions of the scans under anesthesia (first row), awake scans after motion correction (second row), and MRI templates for anatomical reference (third row) for two single rats (Rats 1 and 2) and an interacting rat (Rat 4). Pearson's *r* correlation between relative uptake value (SUVr) for all brain regions ($N = 60$) between the anesthetized and awake scans for (b) Rat 1 and (c) Rat 4.

Fig. 7, the use of the approximate attenuation map should not introduce large errors. For the case of multiple rats' scans, neglecting attenuation correction might introduce bias in the brain activity since the attenuation from the second rat body can be considerable. Therefore, attenuation correction was also performed in the multiple rats' scan. Scatter correction was omitted as it makes little difference in brain quantification in small animal PET scans (Spangler-Bickell et al., 2016).

The current study utilized [^{18}F]FDG to take advantage of its well-established pharmacokinetics to validate the motion-corrected *in vivo* images. Indeed, given that the trace uptake reaches a plateau after an awake uptake period, the awake scans can be compared to the subsequent anesthesia scans. Due to the differences in image noise levels and small changes in tracer uptake over time, some differences in [^{18}F]FDG brain uptake between motion-free and motion-corrected reconstructions

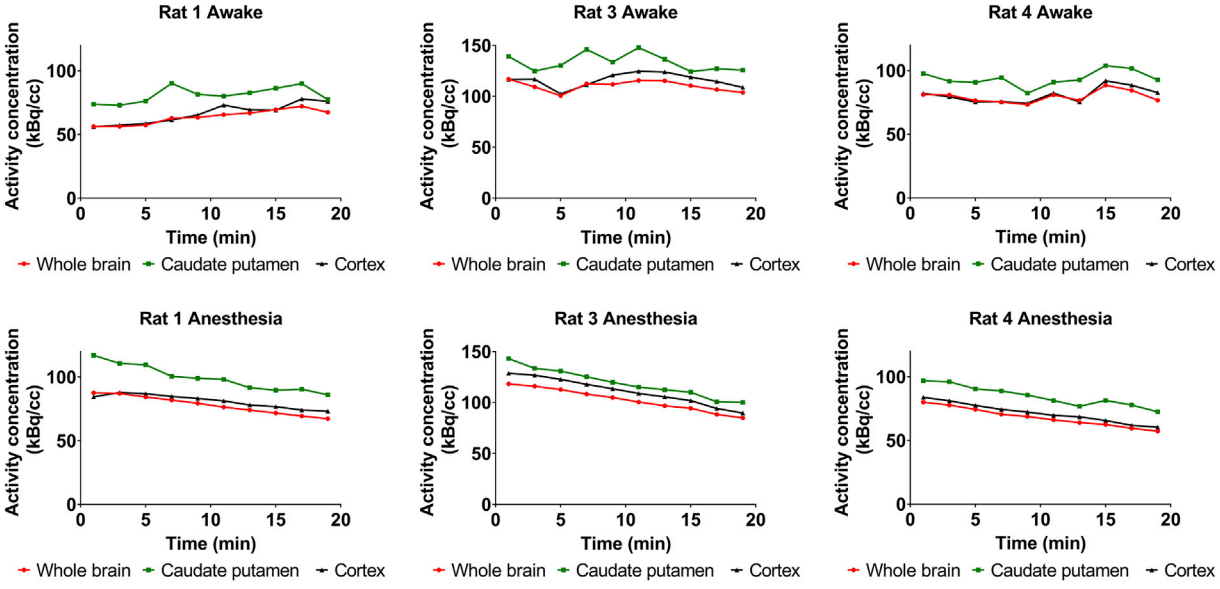

Fig. 8. Time activity curves (TACs) for the whole brain, caudate putamen and cortex during the awake and under anesthesia scans for Rat 1, Rat 3 and Rat 4. First row shows awake scans and second row under anesthesia scans. Time 0 in awake scans is approximately 30 min after tracer injection. Activity in anesthesia TACs is decay corrected to the time point corresponding to the start of the awake scans.

are to be expected. As it can be seen in Fig. 8, [^{18}F]FDG brain uptake in awake scans tend to increase or remain constant, while in the subsequent anesthesia scans a decrease (wash-out) was observed, explained by the use of anesthesia (Miranda et al., 2018) and the different scan start time from injection time (Spangler-Bickell et al., 2016). Nevertheless, the motion-corrected and motion-free reconstructions of the rats' brains showed much similarity in the uptake shape. In addition, a strong and highly significant correlation was obtained for all of the rats in relative regional brain quantification between the motion-corrected and motion-free scans. Factors that might introduce variability between animal's brain uptake in the current study are differences in fasting periods between animals, glucose levels (Deleye et al., 2014) and the periods of anesthesia (Miranda et al., 2018). These factors need to be controlled in future biological studies.

Although the non-reversible tracer [^{18}F]FDG was used for validation purposes, reversible tracers, such as [^{11}C]raclopride, are more relevant for awake rat brain PET studies. To study the time dynamics, these tracers require injection of the animal while it is inside the PET scanner. This can for instance be done using an injection line placed on a swivel (Kyme et al., 2018). Future studies will consider these dynamic scanning protocols using the tracking and reconstruction methods validated in this paper.

The present work opens the way to new experimental designs of small animal PET imaging. For example, the larger area on which the animal can move can be exploited to perform complex behavior and interaction studies. In addition, the absence of anesthesia makes the use of external stimuli during the experiment possible.

5. Conclusions

PET brain scan of awake interacting rats was successfully implemented on the HRRT scanner. Motion corrected reconstructions of a resolution phantom showed excellent spatial resolution in comparison with motion-free reconstructions. In [^{18}F]FDG animal studies, scanning either single or two interacting awake rats, regional brain uptake in the motion corrected reconstructions showed high correlation with that in the motion-free reconstructions brain. The current method opens the way to new small animal brain PET experimental design.

Declarations of interest

None.

Acknowledgments

We express gratitude to Hung-Hsin (Chris) Hsiao in helping with the scanning procedures as well as to the Montreal Neurological Institute and Douglas Research Mental Health Institute materials workshops in their aids to build the scanning cage.

Appendix A. Supplementary data

Supplementary data to this article can be found online at https://doi.org/10.1016/j.neuroimage.2019.02.064.

Funding

The project was funded by a research project (G0A8517N) and research grant (1520217N) from the Research Foundation Flanders, and a research grant (KP) from the University Research Fund (BOF) of the University of Antwerp. In addition, this work was supported by the Weston Brain Institute, Canadian Institutes of Health Research (CIHR; MOP-11-51-31) (to P.R.N.), the Alzheimer's Association (NIRP-12-259245) (to P.R.N.), the Alzheimer Society Research Program and Canadian Consortium on Neurodegeneration in Aging (CCNA) scholarship, and Fonds de Recherche du Québec—Santé (FRQS; Chercheur Boursier) (to P.R.N.). P.R.N. is a member of the CIHR–CCNA Canadian Consortium of Neurodegeneration in Aging.

References

Angelis, G., Bickell, M., Kyme, A., Ryder, W., Zhou, L., Nuyts, L., Meikle, S., Fulton, R., 2013. Calculated attenuation correction for awake small animal brain PET studies. In: 2013 Ieee Nuclear Science Symposium and Medical Imaging Conference. Nss/Mic. https://doi.org/10.1109/NSSMIC.2013.6829263.

Besl, P.J., Mckay, N.D., 1992. A method for registration of 3-D shapes. IEEE Trans. Pattern Anal. Mach. Intell. 14, 239–256. https://doi.org/10.1109/34.121791.

de Jong, H.W., van Velden, F.H., Kloet, R.W., Buijs, F.L., Boellaard, R., Lammertsma, A.A., 2007. Performance evaluation of the ECAT HRRT: an LSO-LYSO double layer high resolution, high sensitivity scanner. Phys. Med. Biol. 52, 1505–1526. https://doi.org/10.1088/0031-9155/52/5/019.

Deleye, S., Verhaeghe, J., wyffels, L., Dedeurwaerdere, S., Stroobants, S., Staelens, S., 2014. Towards a reproducible protocol for repetitive and semi-quantitative rat brain imaging with (18) F-FDG: exemplified in a memantine pharmacological challenge. Neuroimage 96, 276–287. https://doi.org/10.1016/j.neuroimage.2014.04.004.

Gonzalez, R.C., Woods, R.E., 2002. Digital Image Processing, second ed. Prentice Hall, Upper Saddle River, N.J.

Jespersen, B., Knupp, L., Northcott, C.A., 2012. Femoral arterial and venous catheterization for blood sampling, drug administration and conscious blood pressure and heart rate measurements. JoVE. https://doi.org/10.3791/3496.

Kyme, A.Z., Angelis, G.I., Eisenhuth, J., Fulton, R.R., Zhou, V., Hart, G., Popovic, K., Akhtar, M., Ryder, W.J., Clemens, K.J., Balleine, B.W., Parmar, A., Pascali, G., Perkins, G., Meikle, S.R., 2018. Open-field PET: simultaneous brain functional imaging and behavioural response measurements in freely moving small animals. Neuroimage 188, 92–101. https://doi.org/10.1016/j.neuroimage.2018.11.051.

Kyme, A.Z., Zhou, V.W., Meikle, S.R., Fulton, R.R., 2008. Real-time 3D motion tracking for small animal brain PET. Phys. Med. Biol. 53, 2651–2666. https://doi.org/10.1088/0031-9155/53/10/014.

Miranda, A., Glorie, D., Bertoglio, D., Vleugels, J., Debruyne, G., Stroobants, S., Staelens, S., Verhaeghe, J., 2018. Awake (18)F-FDG PET imaging of memantine-induced brain activation and test-retest in freely running mice. J. Nucl. Med. https://doi.org/10.2967/jnumed.118.218669.

Miranda, A., Staelens, S., Stroobants, S., Verhaeghe, J., 2017. Fast and accurate rat head motion tracking with point sources for awake brain PET. IEEE Trans. Med. Imaging 36, 1573–1582. https://doi.org/10.1109/TMI.2017.2667889.

Mizuma, H., Shukuri, M., Hayashi, T., Watanabe, Y., Onoe, H., 2010. Establishment of in vivo brain imaging method in conscious mice. J. Nucl. Med. 51, 1068–1075. https://doi.org/10.2967/jnumed.110.075184.

Otsu, N., 1979. A threshold selection method from gray-level histograms. IEEE Transactions on Systems, Man, and Cybernetics 9, 62–66. https://doi.org/10.1109/TSMC.1979.4310076.

Parker, D.J., Broadbent, C.J., Fowles, P., Hawkesworth, M.R., Mcneil, P., 1993. Positron emission particle tracking - a technique for studying flow within engineering equipment. Nucl. Instrum. Methods Phys. Res. Sect. A Accel. Spectrom. Detect. Assoc. Equip. 326, 592–607. https://doi.org/10.1016/0168-9002(93)90864-E.

Rahmim, A., Bloomfield, P., Houle, S., Lenox, M., Michel, C., Buckley, K.R., Ruth, T.J., Sossi, V., 2004a. Motion compensation in histogram-mode and list-mode EM reconstructions: beyond the event-driven approach. IEEE Trans. Nucl. Sci. 51, 2588–2596. https://doi.org/10.1109/Tns.2004.835763.

Rahmim, A., Lenox, M., Reader, A.J., Michel, C., Burbar, Z., Ruth, T.J., Sossi, V., 2004b. Statistical list-mode image reconstruction for the high resolution research tomograph. Phys. Med. Biol. 49, 4239–4258.

Reader, A.J., Julyan, P.J., Williams, H., Hastings, D.L., Zweit, J., 2003. EM algorithm system modeling by image-space techniques for PET reconstruction. IEEE Trans. Nucl. Sci. 50, 1392–1397. https://doi.org/10.1109/Tns.2003.817327.

Rusu, R.B., Cousins, S., 2011. 3D Is Here: Point Cloud Library (PCL). 2011 Ieee International Conference on Robotics and Automation (Icra).

Schiffer, W.K., Mirrione, M.M., Biegon, A., Alexoff, D.L., Patel, V., Dewey, S.L., 2006. Serial microPET measures of the metabolic reaction to a microdialysis probe implant. J. Neurosci. Methods 155, 272–284. https://doi.org/10.1016/j.jneumeth.2006.01.027.

Schulz, D., Southekal, S., Junnarkar, S.S., Pratte, J.F., Purschke, M.L., Stoll, S.P., Ravindranath, B., Maramraju, S.H., Krishnamoorthy, S., Henn, F.A., O'Connor, P., Woody, C.L., Schlyer, D.J., Vaska, P., 2011. Simultaneous assessment of rodent behavior and neurochemistry using a miniature positron emission tomograph. Nat. Methods 8, 347–352. https://doi.org/10.1038/nmeth.1582.

Spangler-Bickell, M.G., de Laat, B., Fulton, R., Bormans, G., Nuyts, J., 2016. The effect of isoflurane on (18)F-FDG uptake in the rat brain: a fully conscious dynamic PET study using motion compensation. EJNMMI Res. 6, 86. https://doi.org/10.1186/s13550-016-0242-3.